ACI MATERIALS JOURNAL TECHNICAL PAPER

Title no. 95-M60

Analysis of Compressive Stress-Induced Cracks in Concrete



by Kamran M. Nemati, Paulo J. M. Monteiro, and Karen L. Scrivener

This paper presents the results of experimental studies of the micromechanical behavior of concrete under different loading conditions. Cylindrical specimens of normal- and high-strength concrete were tested under uniaxial and confined compression. Cracks and pores in the concrete specimens were impregnated with an alloy that has a low melting point. At the stress of interest, this alloy was solidified to preserve the stress-induced microcracks as they exist under load and images from the cross sections of the concrete specimens obtained using scanning electron microscopy (SEM). Stereological analysis that interprets three-dimensional structures by means of two-dimensional sections was used on the computerized images to determine the density, orientation, and branching of the compressive stress-induced microcracks and the effect of confinement on microcrack behavior. The density and branching of the microcracks decreased as the confining stress increased. The confining stress had a pronounced influence on microcracks in the interfacial transition zone (ITZ) between the cement paste and aggregate. The amount of interfacial cracking decreased significantly as the confining stress was increased. Under uniaxial compression there were significant differences in the crack patterns observed in normal- and high-strength concretes. Under confined conditions the two types of concrete had similar microcrack patterns.

Keywords: compressive stress-induced microcracks; concrete; confinement; image analysis; interfacial transition zone; microcrack branching; microcracks; scanning electron microscopy; stereology; Wood's metal.

RESEARCH SIGNIFICANCE

A special experimental technique has been developed to preserve compressive stress-induced microcracks in concrete as they exist under applied loads, subjected to various loading conditions. Several aspects of crack behavior under load as a function of confinement have been investigated.

INTRODUCTION

Concrete is a heterogeneous, multiphase material. On a macroscopic scale it is a mixture of cement paste and fine and coarse aggregates, with a range of sizes and shapes. On a microscopic scale the cement paste itself is found to be heterogeneous, consisting of unreacted cores of cement grains, crystalline and amorphous hydration products, and porosity.

With regard to its mechanical behavior, concrete is often considered to be a three-phase composite structure, consisting of aggregate particles dispersed in a matrix of cement paste and the transition zone which represents the interfacial region between the particles of coarse aggregate and the hydrated cement paste. The microstructure of cement paste in the vicinity of aggregate particles differs from that of the bulk paste. Many aspects of concrete behavior under stress can be explained by the characteristics and behavior of the cement paste-aggregate interfacial zone. This transition zone, typically 10 to 50 μm thick, is generally weaker than either of the two main components of concrete, and it therefore has a disproportionate influence on the mechanical behavior of concrete compared to its size.

Since the 1920s, researchers have suggested and assumed the existence of different kinds of defects called microcracks that occur in concrete.[1-5] However, only since the early 1960s have such cracks been observed, measured, and characterized in the interior of the system.[6-9] In the 1970s and 1980s the development of nonlinear fracture mechanics models enabled the structure and behavior of concrete to be taken into account. In the 1980s and 1990s, further research has led to the increasingly common application of fracture mechanics in the design of beams, anchorage, and large dams. In spite of this, the theory of fracture mechanics in concrete is not yet as mature as continuum theories, such as elasticity, viscoelasticity, and thermal problems. This is in part due to the limited understanding of the formation and propagation of microcracks in concrete.

Several methods have been used to study the microcracking of concrete. These include acoustic emission,[2,3,10-12] sonic testing,[13,14] microscope technique with dye,[8,9] mercury intrusion porosimetry,[15] x-ray technique,[16-19] optical and electron microscopy computerized tomography analysis,[20] and holographic interferometry.[21-23] Some of these techniques cannot make adequate observations over large areas, are limited in their resolution, or are not sensitive in detecting cracks. Other methods cannot examine the specimens while they are under load, or, in some cases, require special

ACI Materials Journal, V. 95, No. 5, September-October 1998.

Received June 23, 1997, and reviewed under Institute publication policies. Pertinent discussion will be published in the July-August 1999 *ACI Materials Journal* if received by April 1, 1999.

ACI member **Kamran M. Nemati** *is a postdoctoral research fellow at the University of California at Berkeley, and will assume an associate professor position at the University of Washington in Seattle beginning September 1998. He received his PhD in civil engineering from the University of California at Berkeley. His research interests are in fracture mechanics of concrete, microstructural studies of concrete behavior under applied stresses, and experimental methods leading to preservation of cracks in concrete under load.*

ACI member **Paulo J. M. Monteiro** *is Professor and Vice-Chair of Civil Engineering at the University of California at Berkeley, where he received his PhD. He held the Roy W. Carlson Distinguished Professorship at UCB during 1987-88. In 1989 he received the Presidential Young Investigator Award from the National Science Foundation. His research interests include mathematical modeling and microstructure of concrete and testing methods.*

Karen L. Scrivener *received her degree in metallurgy and materials science at Cambridge University. In 1995 she joined the Central Research Laboratories of Lafarge as Senior Scientist in charge of research on calcium aluminate cements.*

preparation of the specimen, which can alter the behavior of the material. The experimental technique described in this paper involves the application of an alloy, called Wood's metal, in the liquid phase, which makes possible the preservation of the microstructure of stress-induced microcracks in concrete as they exist under load.

Wood's metal has been used in the past few years to determine the microstructure of different materials: for example, to study the porosimetry and to measure contact areas and voids between the surfaces of natural fractures,[24] to study the fracture of rocks,[25] and to fill voids and microcracks in clastic rock specimens during loading and solidified it before unloading to preserve the microstructure in specimens under load.[26]

Wood's metal, which has a melting point below the boiling point of water, is used in conjunction with scanning electron microscopy (SEM) and allows the detailed observation of microcracks in concrete as they exist under load. The concept of stereology, which deals with the interpretation of three-dimensional structures by means of their two-dimensional sections, can be applied to analyze the SEM images. Stroeven,[27-30] Ringot,[31] and Massat et al.[32] successfully applied the concept of stereology to study micromechanical aspects of concrete. With the advent of modern image analysis systems, it is now possible to perform stereological analysis on a great number of images accurately and expeditiously.

This investigation tested concrete cylinders of normal- and of high-strength concrete in compression with various degrees of lateral confinement. While under load, the specimens were impregnated with Wood's metal to preserve the induced cracks. After the metal solidified, sections were cut from the specimens and examined in a scanning electron microscope. Image analysis and stereology were used to characterize the quantity and distribution of cracks. The objectives were to determine the shapes and geometry of stress-induced microcracks as they exist under load and to assess how the density, length, orientation, localization and behavior of microcracks depend upon the concrete type and confining stresses.

EXPERIMENTAL TECHNIQUE

The test equipment created to preserve the cracks under applied load is described in detail elsewhere.[33-38]

Five normal-strength and three high-strength concrete cylinders, 8 in. (203 mm) long by 4 in. (102 mm) in diameter, were cast with the mix designs shown in Table 1. The cylinders were cured for about one year in 100 percent humidity and a temperature of 23 C.

The concrete cylinder ends were ground parallel to one another. Water was used as the cooling fluid during cutting and grinding. The confining stress used to generate triaxial compression was supplied by stainless steel wires, 0.041 in. (0.3 mm) in diameter, that were wound around the concrete cylinders at a pre-tension of 130 kN (150 lbf). In the partially confined case the wire was wound one third of the way from each end at a pitch of winding of 4 pitches/cm (10 pitches/in.) for Experiment No. 3, at a pitch of winding of 8 pitches/cm (20 pitches/in.) for Experiment No. 4, and along the entire length at a pitch of winding of 8 pitches/cm (20 pitches/in.) in the fully confined case. Fig. 1 represents the normal-strength concrete specimens used in Experiments 1 through 5. The high-strength concrete specimens used in Experiments 6, 7, and 8 resemble the specimens used in Experimens 1, 2, and 3, respectively.

Wood's metal is a fusible alloy, that is solid at room temperature, with a melting range from 160 to 190 F (71.1 to 87.8 C). In the liquid phase it is nonwetting, with an effective surface tension of about 400 mN/m.[24] It consists of 42.5 percent bismuth (Bi), 37.7 percent lead (Pb), 11.3 percent tin (Sn), and 8.5 percent cadmium (Cd). Wood's metal has a Young's modulus of 9.7 GPa, a density of 9.4 g/cm^3, and does not go through any volume change during hardening. The advantage of such an alloy is that it can be intruded into voids and stress-induced microcracks while the specimen is held at the desired stress level and then solidified to preserve

Table 1—Concrete mix design

Normal-strength concrete	
Material	Quantity/type
Cement	583 lb/yd^3 (346 kg/m^3)
Water	308 lb/yd^3 (183 kg/m^3)
Coarse aggregate ($^1/_2$ in. maximum size aggregate)	1650 lb/yd^3 (979 kg/m^3)
Sand	1448 lb/yd^3 (859 kg/m^3)
High-range water-reducing admixture	15 oz/100 lb cement (10 ml/kg)
w/c	0.528
Slump	1.5 in. (38 mm)
Average strength	6200 psi (51.7 MPa)
High-strength concrete	
Material	Quantity/type
Cement Type I/II	600 lb/yd^3 (356 kg/m^3)
Rice husk ash	90 lb/yd^3 (53 kg/m^3)
Crushed limestone ($^3/_8$ in. maximum size aggregate)	1760 lb/yd^3 (1044 kg/m^3)
Top sand (FM = 3.0)	1325 lb/yd^3 (768 kg/m^3)
Water	215 lb/yd^3 (128 kg/m^3)
Superplasticizer	5.7 l/m^3
w/c	0.358
Slump	1 in. (25 mm)
Average strength	11,000 psi (75.8 MPa)

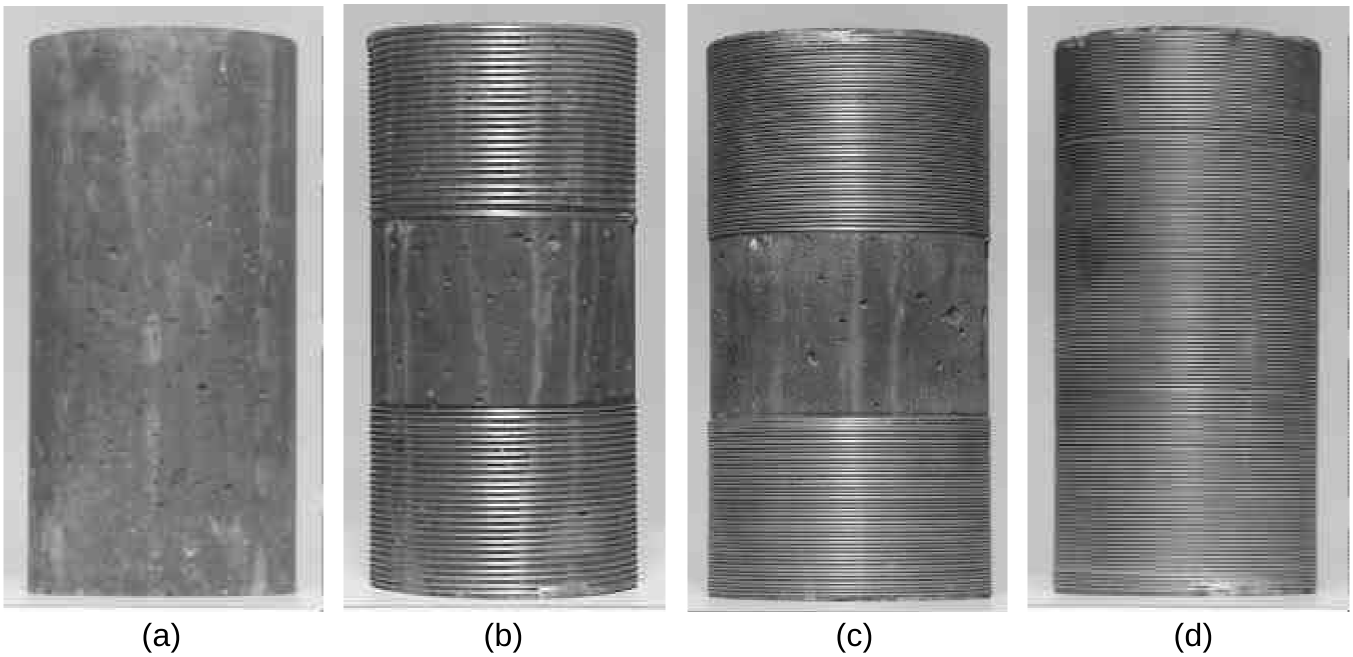

Fig. 1—Normal-strength concrete specimens used in the experiments: (a) Experiments No. 1 and 2, no-load and uniaxial tests; (b) Experiment No. 3, partially confined (1) test; (c) Experiment No. 4, partially confined (2) test; and (d) Experiment No. 5, fully confined test.

the geometry of the microcracks induced. The concrete cylinders were first dried in an oven at a temperature of 110 F (43.3 C). This removed the moisture in the concrete and preheated the cylinder, ensuring that the molten metal alloy could penetrate into pores and cracks deep within its core without solidifying prematurely.

A total of eight experiments, five of normal-strength and three of high-strength concrete cylinders, were conducted with conditions as defined in Table 2. Each specimen was loaded to a similar point in the stress-strain curve, corresponding to about 80 to 85 percent of the ultimate strength.

One disadvantage to using the Wood's metal method is that the concrete cylinders are dried by pre-heating the specimens at a temperature of about 43 C prior to testing. This process could induce excessive drying, thereby forming shrinkage cracks which may percolate through the sample.

After solidification of the metal each of the cylinders was sectioned along its long axis, using oil as a coolant. One of the half-cylinders was sectioned at the middle along its diameter. An axial slab, approximately $^1/_8$-inch (5 mm) thick, was sliced parallel to the direction of the load. Four sections were extracted from the axial slab (Specimens 1 through 4), two from the mid-line edge, and two from the top surface. In the micrographs each section is identified by a two digit code, the first referring to the experiment number (Table 2) and the second to the section number (Fig. 2). The sections were 1 in. (25 mm)-square and had an approximate thickness of 5 mm.

One side of each section was lapped flat with 120, 220, 320, and 600 grade silicon carbide using a rotating grinder and then mounted against a 1 in. (25 mm)-diameter glass plate with epoxy. A parallel-sided slice, 2 to 3 mm thick, was then cut from the section with a diamond slicing wheel and a nonaqueous lubricant (propylene glycol coolant). The sections were lapped with a wheel grinder and polished with 600 grade silicon carbide, 100-, 50-, and 10-micron aluminum powder and 5-, 3-, and $^1/_4$-micron diamond paste. After each stage of polishing, the specimens were immersed in acetone and placed in an ultrasonic bath.

The specimens were examined using a JEOL JSM-35CF scanning electron microscopy (SEM) in conjunction with an image analyzer.

STEREOLOGICAL RELATIONSHIPS

Stereology deals with the interpretation of three-dimensional structures by means of their two-dimensional sections. There are various approaches to stereological problems. The statistico-geometrical approach depends on measuring and classifying a large number of two-dimensional images and is the method utilized in this study. It is applicable when objects are randomly distributed in space. In such cases valid results may be obtained from a single section, if this is extensive enough to contain a statistically significant number of features and is representative of the bulk specimen.

Fundamental expressions have been determined which relate measurements on two-dimensional sections to the three-dimensional structure. Table 3 presents some of the symbols commonly used relevant to this work.

The relationships between L_A and S_V with P_L are presented below[39]

Surface area per unit volume, S_V

$$S_V = 2P_L \quad \mu m^2/\mu m^3 \tag{1}$$

Length of line per unit area, L_A

Table 2—Experiments conducted

Experiment no.	Loading condition	Concrete strength	Load, psi/MPa	Ultimate load, percent
1	No load	Normal	1500/10.3*	N/A
2	Uniaxial	Normal	5000/34.5	80
3	Partially confined 1†	Normal	6000/41.4	81
4	Partially confined 2‡	Normal	6000/41.4	82
5	Fully confined	Normal	7330/50.6	84
6	No load	High	1500/10.3*	N/A
7	Uniaxial	High	9350/64.5	85
8	Partially confined	High	10,800/74.5	82

* Restraining load to prevent movement of the specimen during impregnation.
† Pitch detail: pitch of winding of 4 pitches/cm (10 pitches/in.).
‡ Pitch detail: pitch of winding of 8 pitches/cm (20 pitches/in.).

$$L_A = \left(\frac{\pi}{2}\right)P_L \quad \mu m/\mu m^2 \tag{2}$$

or

$$\frac{\pi}{2}P_L = L_A = \frac{\pi}{4}S_V \tag{3}$$

IMAGE ANALYSIS PROCEDURE

The samples were examined in the scanning electron microscope with backscattered electrons (BSE). The SEM was operated at 15 kv and probe current of around 1 nA at a working distance of 15 mm. The images were acquired by the image analyzer at a magnification of 60× and digitized into an array of 512 x 512 pixels, with 255 gray levels (1 pixel = 3.3 μm); 55 images were extracted from each sample. A typical gray level BSE image is shown in Fig. 3.

Fig. 4 shows a histogram of the distribution of gray levels in the BSE image superimposed on the original image. As the average atomic number of the Wood's metal is much higher than cement paste and the aggregates, impregnated cracks and pores can be easily distinguished in the BSE image. This technique also avoids the problem of crack formation during specimen preparation. The peak at the right (high gray level) corresponds to the areas of Wood's metal, while the peaks to the left correspond to the cementitious phases and aggregate. This histogram was used to select the threshold value for discriminating the areas of Wood's metal, shown in Fig. 5.

The image shown in Fig. 6 includes small isolated pores, which were eliminated by the application of a minimum size threshold (scrap) for objects of 10 pixels (minimum feature size of approximately 33 μm).

Next, a skeletonized binary image was obtained by binary thinning. For every thinning step, pixels that are not relevant to the connectivity of an object are removed from the object margins, i.e., converted into background pixels, thus connectivity of objects is maintained. This process was continued until all objects were reduced to a width of one pixel that approximates the skeleton. Fig. 7 is the final binary image used for stereological measurements.

To quantify the crack orientation, the skeletonized image in Fig. 7 was then intersected by an array of straight parallel lines at 15 deg angular increments, in this case at angles of 0,

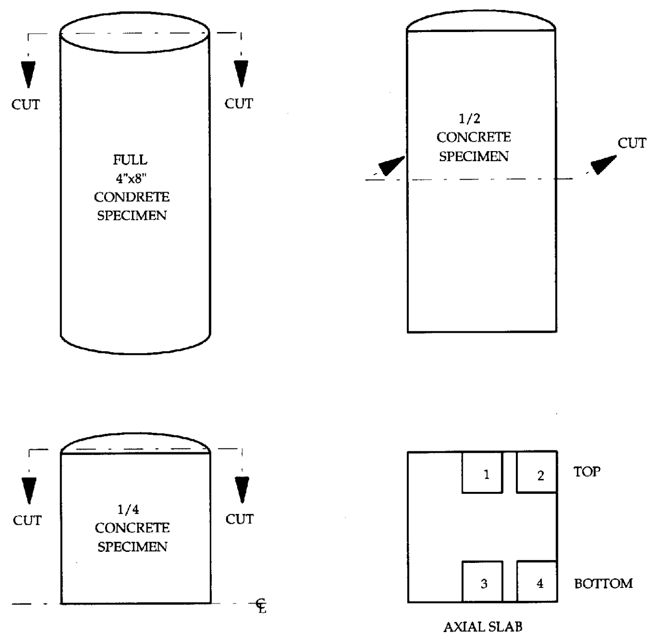

Fig. 2—Specimen extraction and numbering scheme.

15, 30, 45, 60, 75, 90, 105, 120, 135, 150, and 165 deg to the compression axis (Fig. 8). At each angle the number of intersections of the line array with the thinned crack network was measured. A vector of length proportional to the number of intersections $P_L(\theta)$ was plotted at the θ to give a "rose of intersections" diagram, which characterizes the anisotropy of the cracks. Since lines at angle θ + 180 deg are equivalent to those at angle θ, the rose diagrams only cover the range of 0 to 165 deg.

This method allows the anisotropy of the crack pattern to be characterized. For example, if most cracks were oriented parallel to the compression axis the number of intersections with the lines at 0 deg would be highest. Further image analysis procedures are discussed in the next section.

RESULTS

Characterization of microcracks

Normal-strength concrete—Fig. 9 shows typical images from the unloaded specimen. To restrain the specimen during the impregnation with Wood's metal, this specimen was subject to a small uniaxial compressive stress of 1500 psi (10.3 MPa). In this specimen the bright areas that have been

Table 3—List of basic stereological symbols and their definition

Symbol	Dimensions	Definition
P_L	μm^{-1}	Number of intersections per unit length of features (i.e., cracks) in a section with a superimposed array of equally spaced, randomly oriented parallel lines.
$P_L(\theta)$	μm^{-1}	Number of intersection of cracks in a section with an array of equally spaced parallel lines oriented at an angle θ to a reference axis.
L_A	$\mu m / \mu m^2$	Total crack length in a section per unit of area.
S_V	$\mu m^2 / \mu m^3$	Total crack surface area per unit of volume.

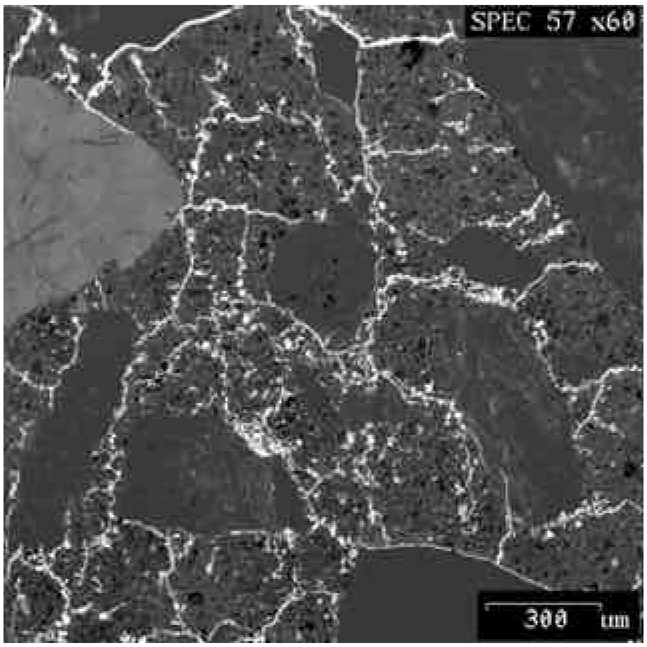

Fig. 3—Typical BSE image.

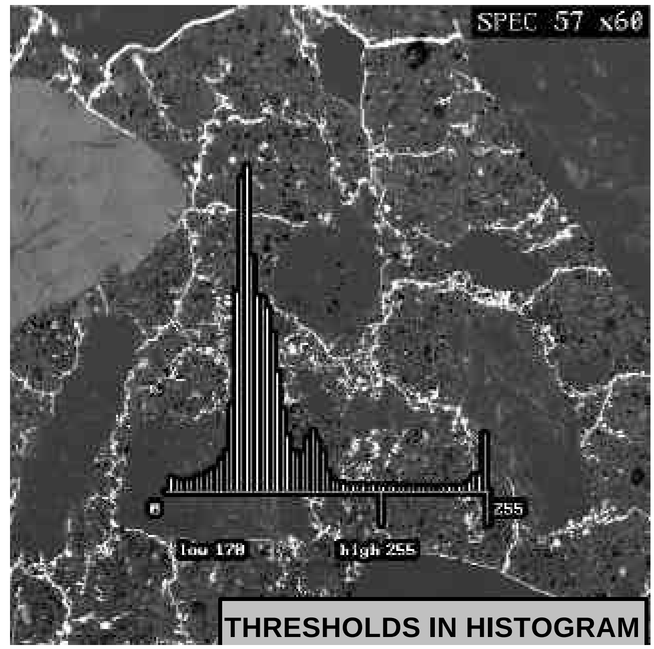

Fig. 4—Establishing threshold in histogram.

permeated by Wood's metal correspond to regions of connected porosity. These regions are most common in the interfacial transition zone around aggregate particles, a finding which is discussed in more detail elsewhere.[35] The connectivity (and hence degree of penetration by Wood's metal) of these pore agglomerations could have been enhanced by the formation of bridging microcracks during the curing of the samples and the drying process prior to loading. There are no long cracks characteristic of stress induced cracking in these images. In contrast such cracks are readily apparent in the samples from the loaded unconfined specimen, shown in Fig. 10.

The microcracks in the loaded specimens appear to have been generated by several different mechanisms. Fig. 11 shows two micrographs taken from the partially confined sample (Experiment No. 3) where microcracks have propagated through the cement paste and along the interfacial transition zone. Many cracks appear to have been generated from voids as a result of local tensile stress tangential to the void boundary, with a value of the order of the maximum applied principal stress. These cracks usually originated from the pore boundaries and propagated in the direction of maximum compression. Fig. 12 shows two micrographs of microcracking around air voids, which are filled with Wood's metal.

Microcracks also appeared to have been generated inside aggregates, with a tendency to run parallel to the compression axis. It is presumed that these aggregates experienced loading across their height leading to a mode of fracture analogous to that which occurs in a splitting tensile test. Fig. 13 shows two micrographs of this phenomenon for the fully confined loading conditions.

High-strength concrete—Compared to normal-strength concrete, high-strength concrete behaves more like a homogeneous material, with its stress-strain curve being steeper, and remains closer to linearity at a higher stress-strength ratio. In addition, fracture in high-strength concrete tends to be characterized more accurately by linear elastic fracture mechanics than does normal-strength concrete.[40] The amount and degree of microcracking in the interfacial transition zone (ITZ) between the cement paste matrix and the aggregates cause a more brittle mode of fracture and less volumetric dilation.[41] Because of densely packed cement grains and a reduced amount of pores and cracks, high-strength concrete has a lower *w/c*, resulting in stronger cement paste. As a consequence, high-strength concrete has a stronger interfacial transition zone, which is due to a reduction in excess bleeding and the filling of gaps by mineral admixtures, in this case, rice husk ash (RHA).

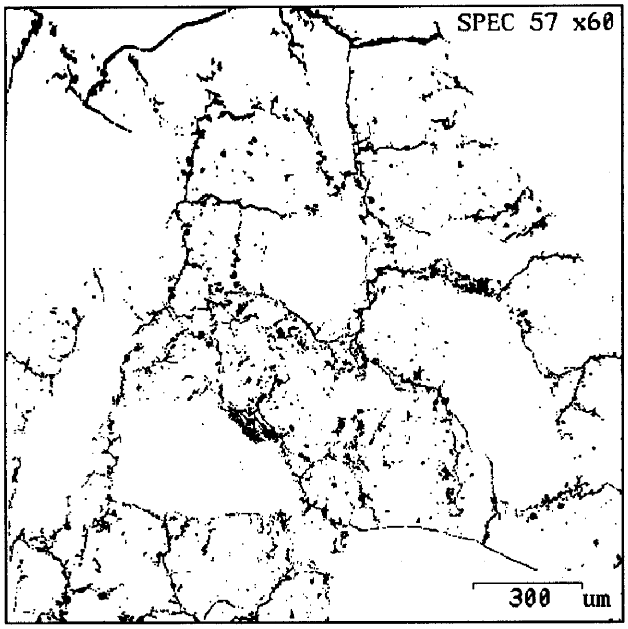

Fig. 5—Threshold image.

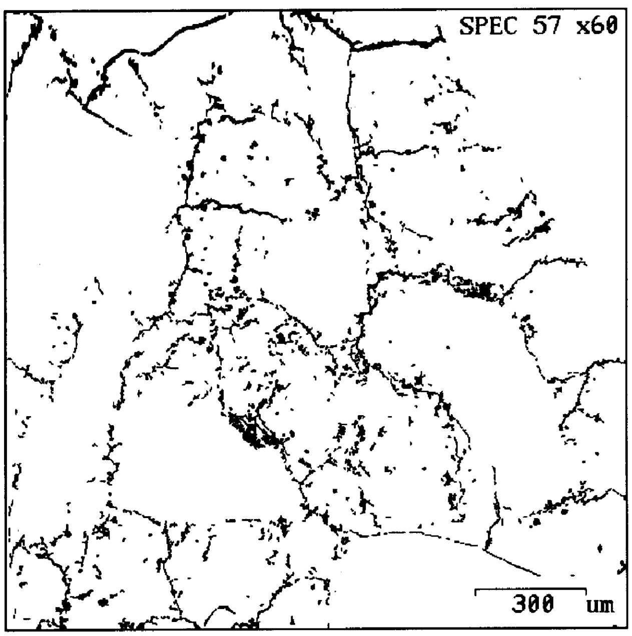

Fig. 6—Crack network image after application of scrap function.

Two SEM micrographs from the unloaded specimen of high-strength concrete are shown in Fig. 14, with no stress-induced microcracks observed in these sections. Regions of connected porosity in the ITZ are also far less apparent, which is due to the refinement of the microstructure in this region.

Fig. 15 shows two SEM micrographs from Experiment No. 7, which was conducted under uniaxial condition. From these micrographs it is clear that less cracking occurs in high-strength than in normal-strength concrete; because of the stronger cement paste, most of this cracking takes place in the interfacial transition zone.

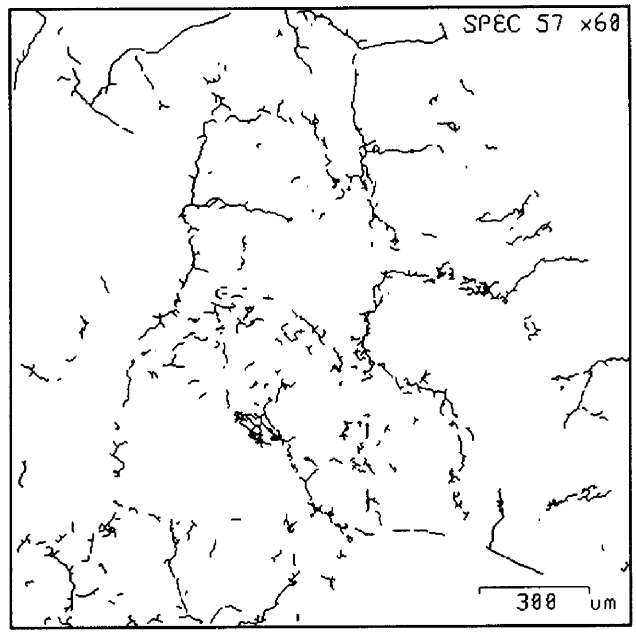

Fig. 7—Binary-thinned image of the crack network in concrete.

Microcrack density distribution

Plots of the cracks surface area per unit volume S_V as a function of confinement are presented in Fig. 16 for normal-strength and high-strength concrete specimens. The value of S_V was obtained based on the average value of P_L in all directions. It is clear that the crack surface area S_V decreases as the confining stress increases for both normal- and high-strength concrete.

As illustrated in Fig. 9, in the unloaded normal-strength sample the Wood's metal penetrates into connected pores, which are then measured as "cracks" by the image analysis program. The samples from the unconfined experiment (No. 2) show a considerable increase in S_V over the unloaded samples. In all the normal-strength confined specimens (Experiments No. 3 through 5) the measured S_V is actually lower than that in the unloaded sample. This may be attributed to the decrease in the amount of connected porosity penetrated by the Wood's metal, either due to the closure of bridging microcracks or to the collapse of pore throats under the confining pressure.

In the high-strength concretes, S_V in the unloaded sample was lower than in the case of the normal-strength concrete. This is due to the decrease in the amount of connected porosity in the ITZ as noted from the micrographs (Fig. 15). There is a dramatic increase in the crack density in the unconfined sample, but again the crack density in the confined sample is much lower. In both uniaxial and confined cases the crack densities in the normal- and high-strength concrete are similar. Although the absolute loads were different, the testing conditions correspond to similar percentage of the ultimate load.

Kranz[42] put forward an explanation for the decrease in crack density in the presence of confinement. Microcracks are generated by local tensile stresses, which depend on the geometry of pores and aggregates, and material heterogeneity, as well as the magnitude and direction of applied

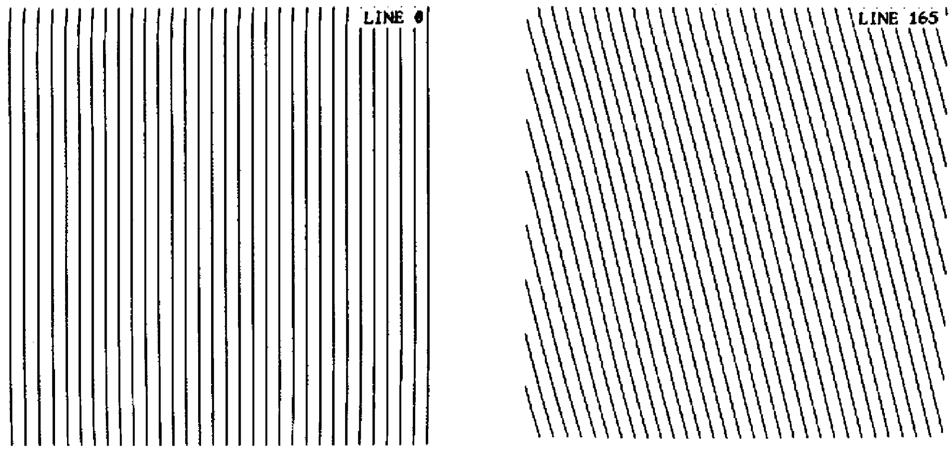

Fig. 8—Array of straight parallel lines at 15 deg angular increments.

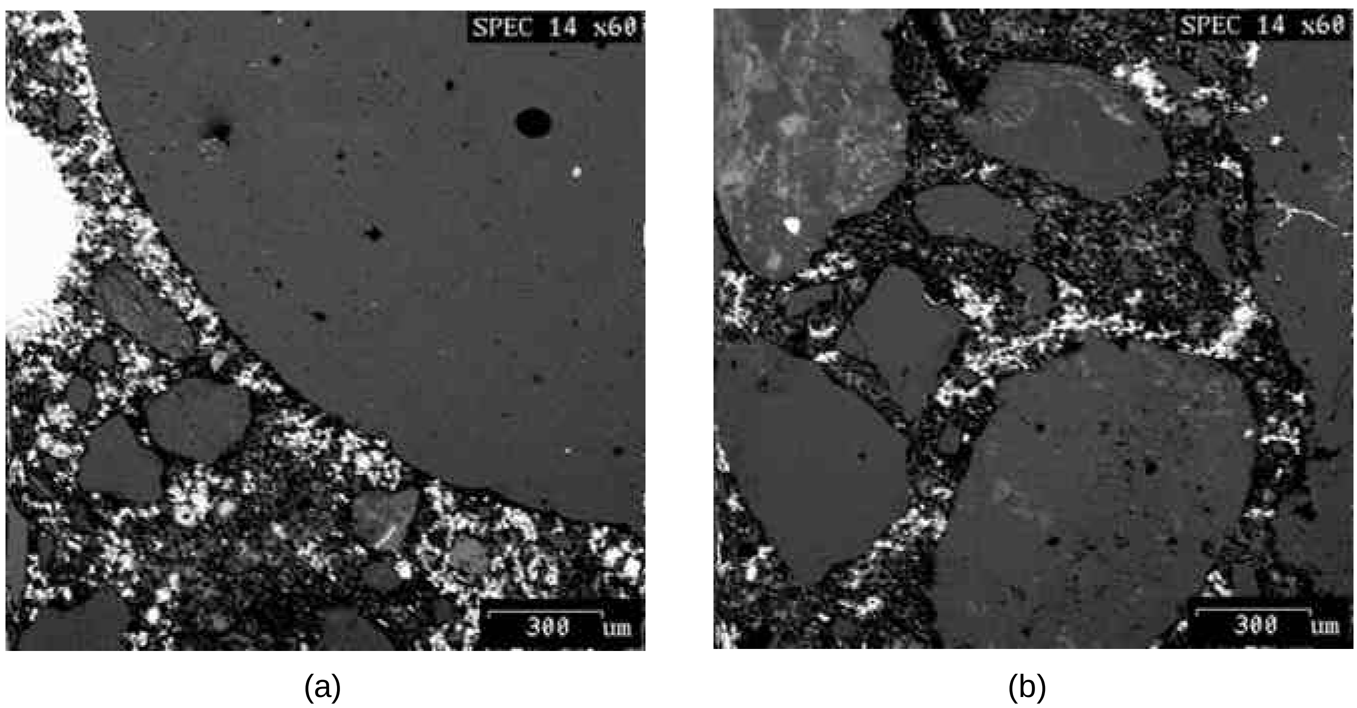

Fig. 9(a) and (b)—SEM micrographs from the no-load experiment.

stresses. Confinement increases the hydrostatic pressure acting on an existing deviatoric stress field, and so is likely to decrease the range and magnitude of deviatoric stresses concentrated near crack tips, as well as increase frictional resistance to shear between crack surfaces in contact. For tensile cracks this increases the energy (and hence stress) required for propagation, thereby making crack growth less probable.

The microcrack density distribution Γ represents the number of microcracks per unit of observation area. Pore spaces were not counted as microcracks. For a body of volume V (unit thickness) containing N cracks with initial cracks of length ℓ_0, the initial crack density parameter Γ is given by

$$\Gamma = \frac{N\ell_0^2}{V} \tag{4}$$

The crack density parameter Γ, in an image of area A with N cracks of length ℓ_i, can be obtained from the following relationship

$$\Gamma = \frac{\sum_{i=1}^{N} \ell_i^2}{A} \tag{5}$$

where

Γ = Crack density parameter
ℓ_i = Crack length (mm)
A = SEM image area (512 x 512 pixels = 2.8358 mm^2)

Fig. 17 illustrates the crack length and crack densities for the partially confined specimens in both confined and unconfined portions of the specimen for Experiments No. 3 and 4 which

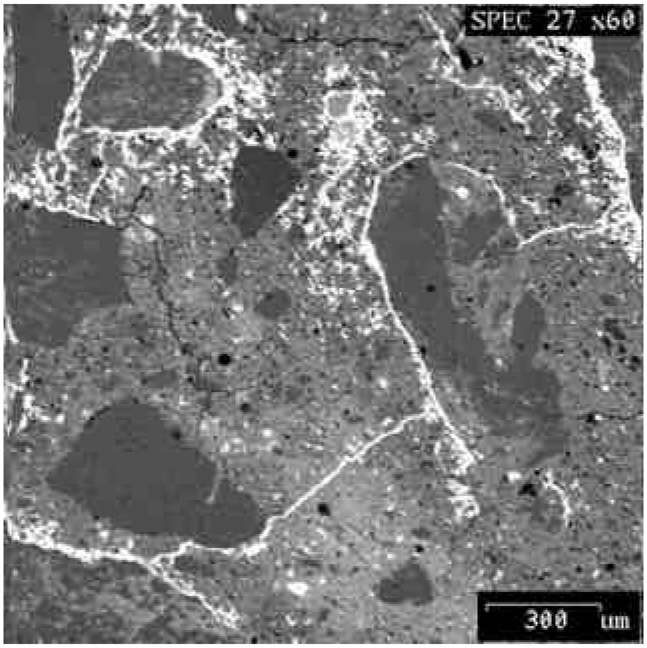

Fig. 10—SEM micrograph from the uniaxial experiment.

were subjected to a confining stress over each end and uniaxial compression over the center. In both cases the crack densities in the center and edge of the sample are smaller in the confined portion than in unconfined portion. Also, in both experiments, the average crack length is smaller in the center portion of the specimen than along the edge.

Orientation of microcracks

Fig. 18 shows the rose of the number of intersections for normal- and high-strength concrete specimens. The degree of orientation obtained for the partially confined specimens were based on the crack patterns observed in the confined portion.

From Fig. 18 it is apparent that on a microscopic scale, the cracking is relatively isotropic. The normal-strength uniaxial section shows some tendency for a higher number of intersections for line arrays oriented parallel to the stress axis, indicating that the cracks in this section tended to run perpendicular to the loading direction. However, this tendency is not present in the normal-strength confined sections. The high-strength concretes show a very slight, probably insignificant, orientation effect in both the uniaxial and confined specimens.

Any tendency to anisotropy of cracking, which might have occurred in a homogeneous material, will be greatly affected by the heterogeneity of concrete. In particular, visual examination makes it clear that a large proportion of the cracks occur at the cement paste/aggregate interfaces, which will be randomly oriented.

Interfacial cracks and pores

Qualitative examination of the sections indicate that the cracking was dominated by cracks at the interface between aggregate and cement paste and by the presence of regions of connected pores in the ITZ.

Investigations have shown that very fine cracks at the interface between coarse aggregate and cement paste exist

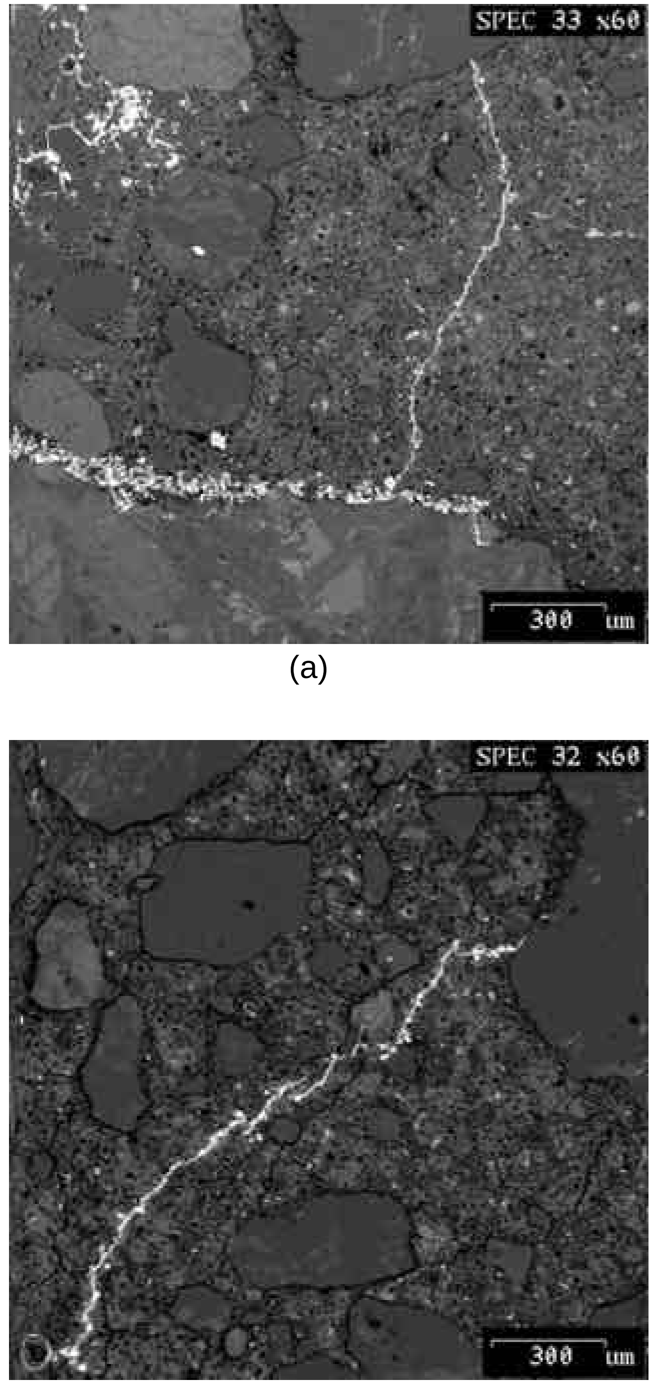

Fig. 11(a) and (b)—SEM micrographs from the partially confined experiment.

even prior to application of the load on concrete.[8] The initiation and propagation of these cracks are considered to be the dominant mechanisms responsible for the nonlinear response of concrete subjected to uniaxial compressive loading. Interfacial cracks remain stable up to about 30 percent or more of the ultimate strength and then begin to increase in length, width, and number. The overall stress under which they develop is sensitive to the *w/c* ratio of the paste. At 70 to 90 percent of the ultimate strength, cracks open through the cement paste and bridge the interfacial cracks, and the continuous crack pattern is formed.[43] Studies con-

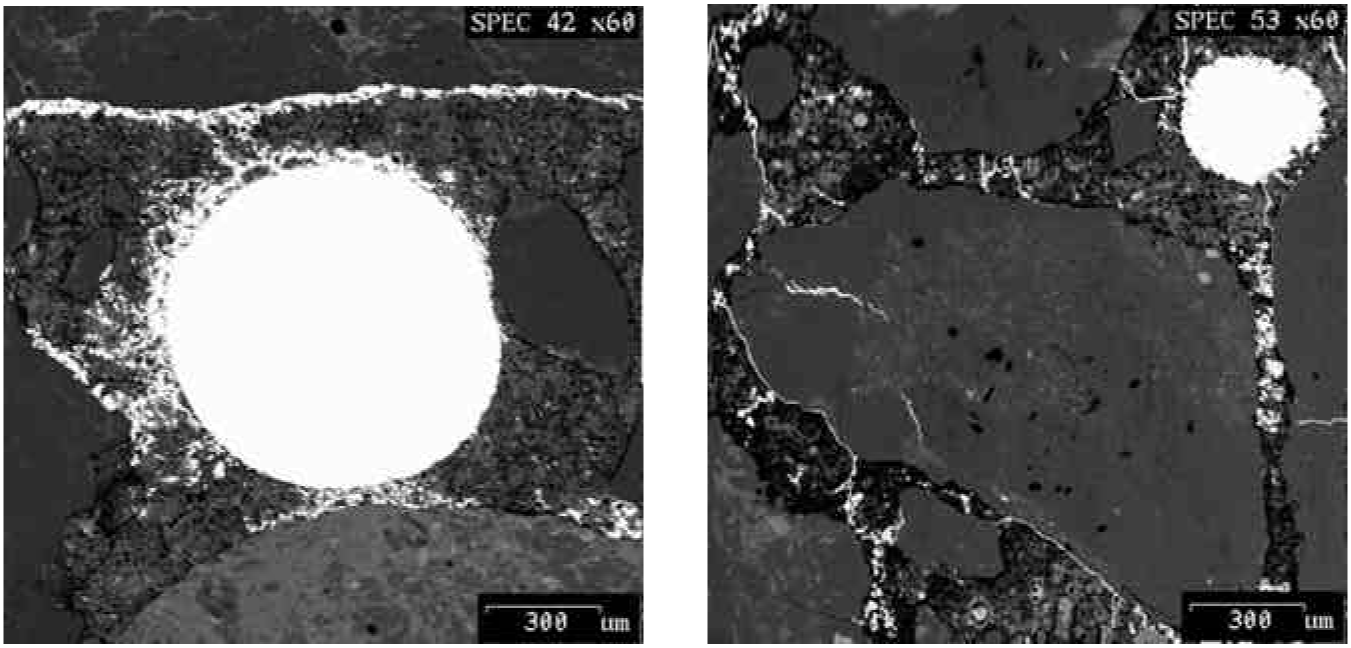

(a) (b)

Fig. 12(a) and (b)—SEM micrographs of microcracks propagating from a pore.

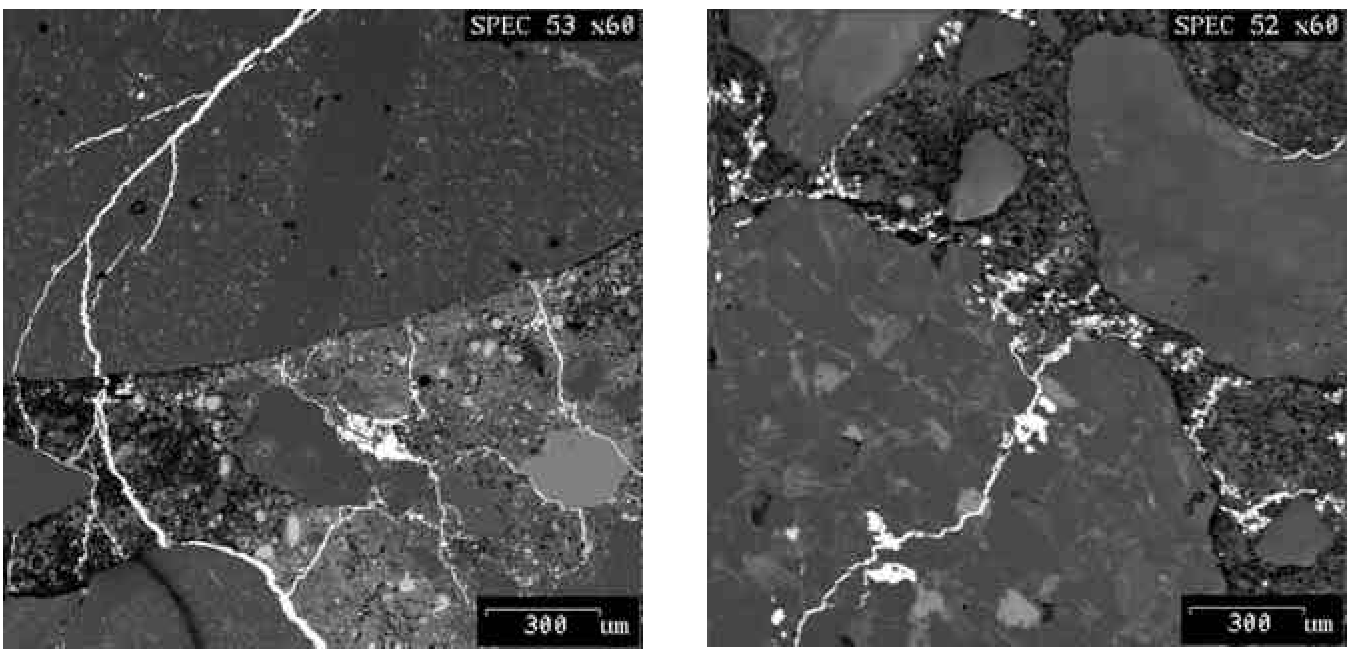

(a) (b)

Fig. 13(a) and (b)—SEM micrographs of aggregate cracking.

ducted using microscopic analysis[8,44,45] reveal that cracks frequently initiate at the interface and then propagate into the matrix where mortar cracks join to form a continuous crack path prior to ultimate load.

To analyze the phenomenon of interfacial pores and cracking, an attempt was made to distinguish these from the matrix cracks. The outline of the aggregate particles in the image was identified by manual tracing. The areas corresponding to the aggregate particles were then dilated by about 13 μm and cracks within this dilated region identified. The length of these interfacial cracks was then calculated as a percentage of the total crack length in the image. Fig. 19 shows the percentage of interfacial microcracks and pores as a function of the confining stress for normal- and high-strength concrete. As shown, there is a sharp reduction in the amount of interfacial microcracks as the confining

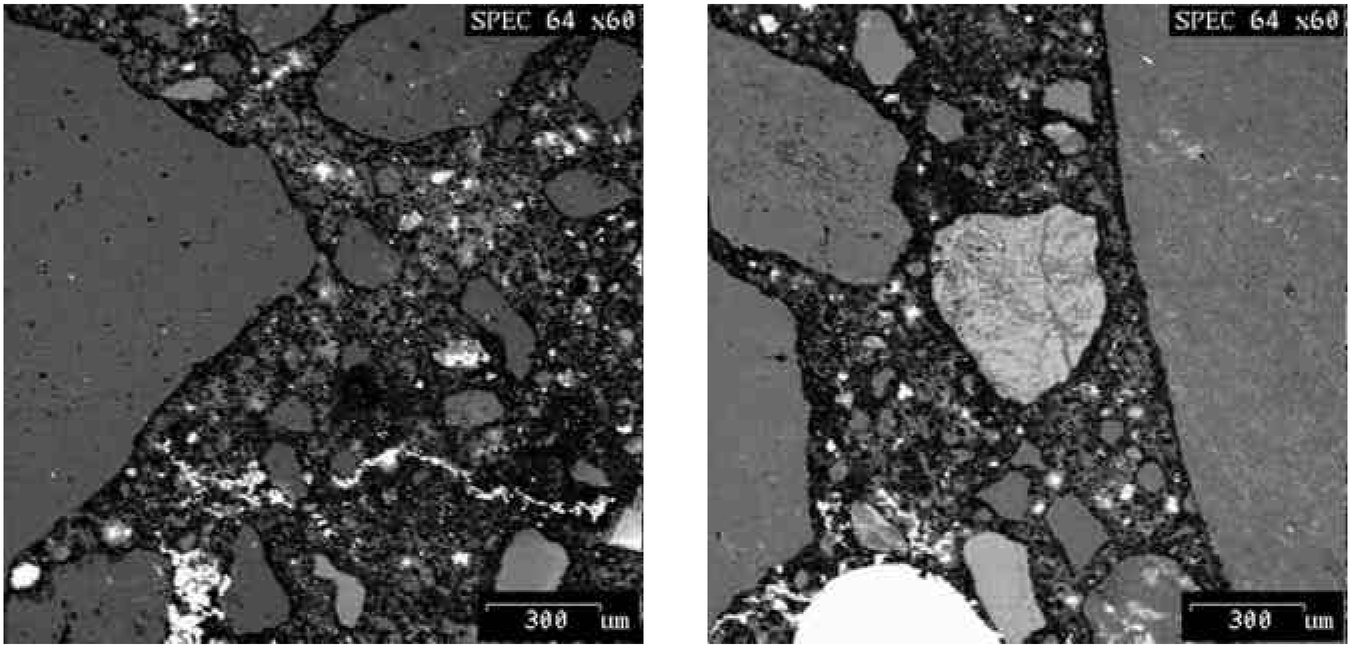

(a) (b)

Fig. 14(a) and (b)—Micrographs of high-strength concrete.

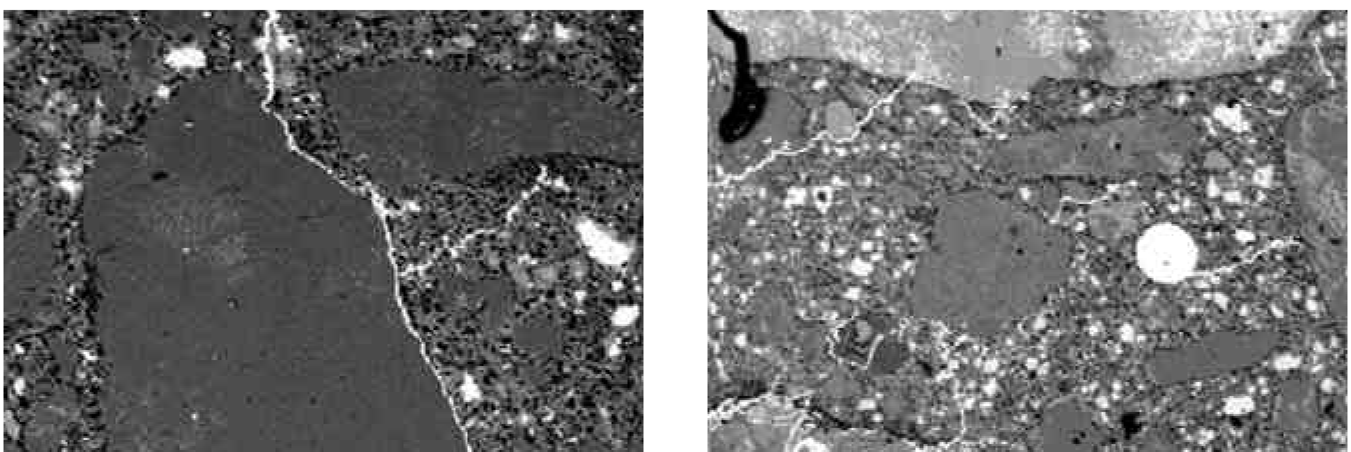

(a) (b)

Fig. 15(a) and (b)—Micrographs of high-strength concrete.

stress increases. The greatest reduction occurred when the concrete specimen was fully confined.

In the case of high-strength concrete, it is apparent that the percentage of interfacial cracks in the unloaded and uniaxially loaded specimens is much lower than in the corresponding of normal-strength concrete specimens. This may be partially explained by the elimination of the region of connected pores that were a common feature of the ITZs of the normal-strength concrete, but also confirms the improvement of the strength of the interfacial zone in the high-strength concrete. In the confined case the percentage of interfacial cracks is similar in the two types of concrete.

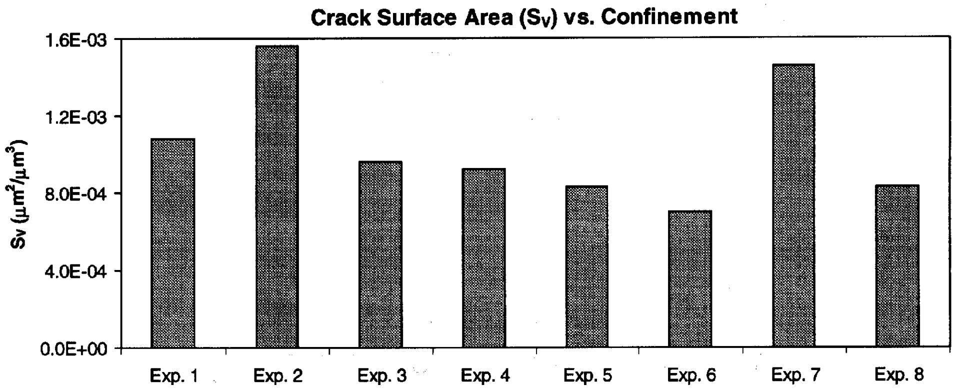

Fig. 16—Crack surface area (S_V) as a function of confinement for normal- and high-strength concrete.

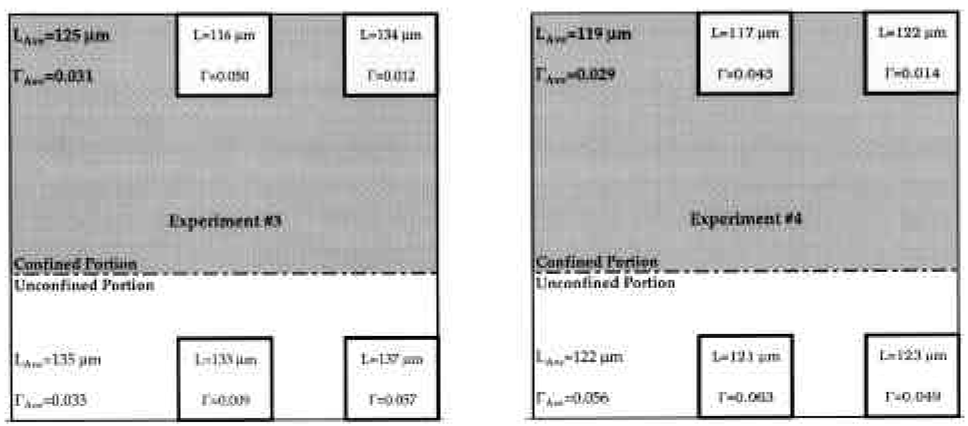

Fig. 17—Diagrammatic representation of crack length and crack density at confined and unconfined portions.

Microcrack branching

Cracks with frequent branching are often observed in the fracture of brittle and quasi-brittle materials, such as ceramics and concrete. The crack-branching patterns of materials are very complex and irregular. However, quantitative analysis of branching patterns could reveal some important information about the stress applied during crack propagation, as well as material characteristics, such as surface energy and the elastic constant.[46,47] Fractal analysis has also been applied to complex branching patterns.[41,42,48]

Since the images being analyzed are a general indication of the crack pattern, they can be considered to be a very broad estimate of crack complexity. Therefore, the crack branching analysis presented here should be considered as a comparative measure between the samples. For this purpose a computer program was developed to measure the number of 3-way and 4-way crack-branching nodes that appeared in the skeletonized images, similar to the ones shown in Fig. 20.

To normalize the number of crack-branching nodes, the number was divided by the crack surface area per unit volume S_V. Fig. 21 shows that as the confining stress increases, the number of crack-branching nodes decreases. This is expected since the propagation of microcracks is controlled by the stress intensity factor at the microcrack tips; as the confining stress increases, the negative stress intensity factor imposed by confinement increases proportionately. This increases the energy required for cracks to grow and branch off. The amount of branching in the high-strength concrete is slightly less than the number of cracks in the normal-strength concrete for the uniaxial loading condition, but similar in the confined case. This can be attributed to the fact that high-strength concrete is more brittle than normal-strength concrete. As a result, when fracture occurs in high-strength concrete, the crack propagation is associated with less branching.

SUMMARY AND CONCLUSIONS

This paper reports on an experimental technique that has been developed to preserve the stress-induced microcracks as they exist under compressive load, by the intrusion and solidification of Wood's metal. This technique was applied to study the behavior of both normal- and high-strength concrete in uniaxial and confined conditions.

By analysis of BSE images and the application of stereology, various measures of the crack density and distribution were obtained: crack surface area per unit volume; crack orientation; average crack length; and crack branching.

In the unloaded normal-strength concrete most of the areas intruded by the Wood's metal were interconnected pores in the ITZs around aggregate particles. These areas were less

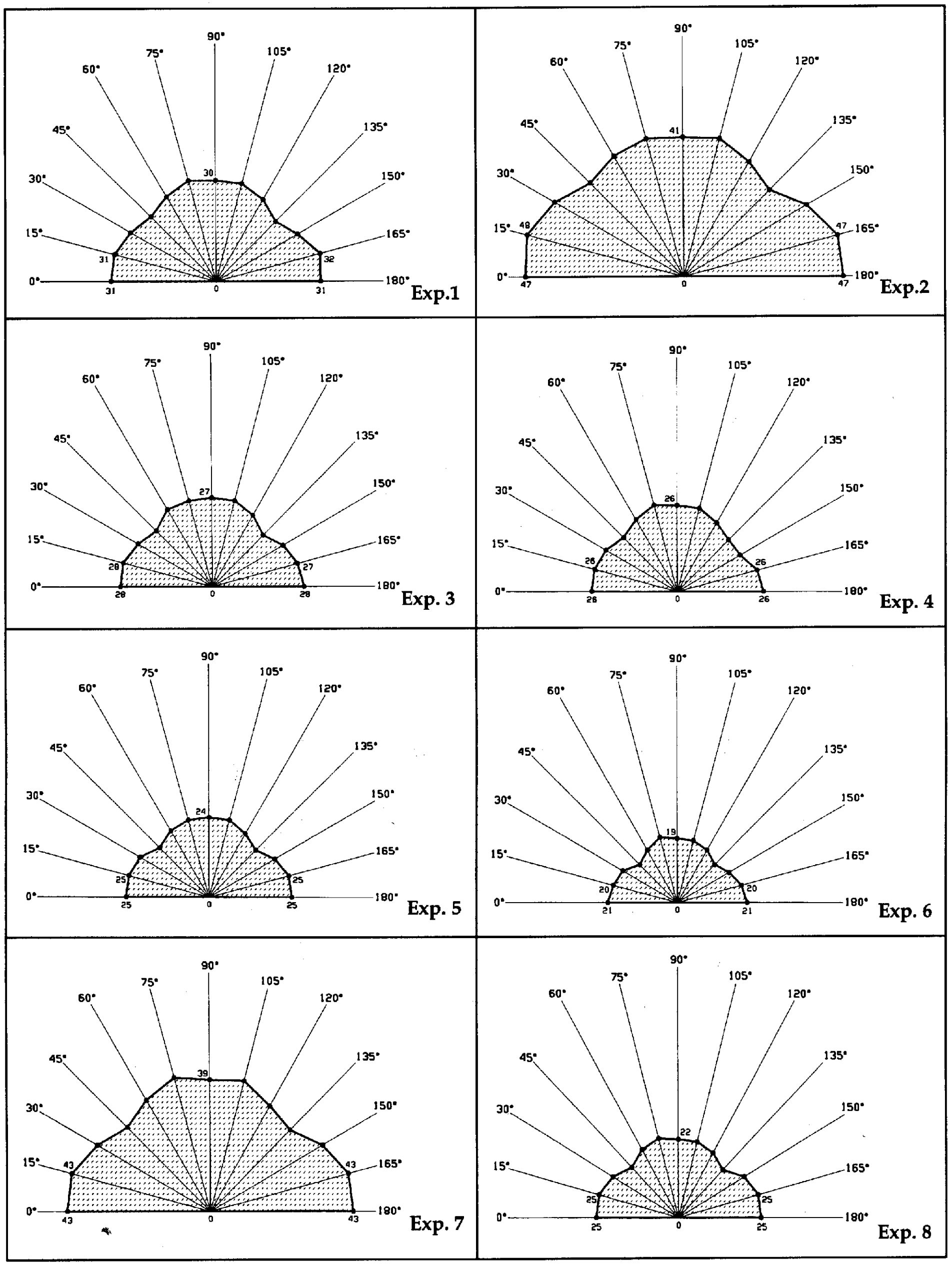

Fig. 18—Rose of the number of intersections diagrams for normal- and high-strength concrete (results of partially confined 1 and 2 conditions are from the confined portion of the specimen).

apparent in the high-strength concrete, confirming the improved microstructure of the ITZ in these concretes.

The measured surface area of cracks increased considerably when the specimens were loaded uniaxially. At similar percentages of the ultimate loads the crack density in the normal- and high-strength concrete were similar.

Confinement dramatically decreased the crack density observed in the loaded samples. In the normal-strength concretes the crack density was lower than in the unloaded samples, as it was more difficult for the Wood's metal to intrude through the ITZs.

Measurements of the orientation indicated that the cracks were relatively isotropic at a microscopic level. This may be partly due to the domination of interfacial cracks, which must be randomly oriented.

In the unloaded and uniaxially loaded specimens the percentage of interfacial cracks was much higher in the normal-strength than in the high-strength concrete. Confinement decreased the percentage of interfacial cracks to a similar level for both types of concrete.

For uniaxial loading the cracks were less branched in the high-strength concrete. Confinement reduced the level of crack branching per unit length of crack for both types of concrete.

The crack densities in the center and edge were smaller in the confined portion than in unconfined portion. In the same

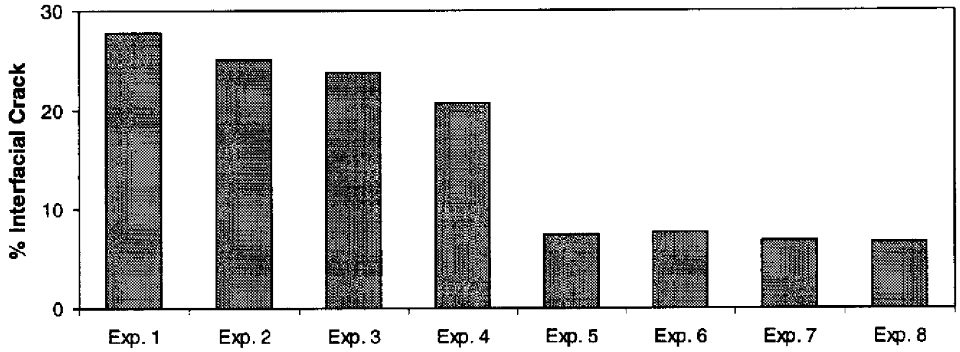

Fig. 19—Effect of confinement on interfacial microcracks of normal- and high-strength concrete.

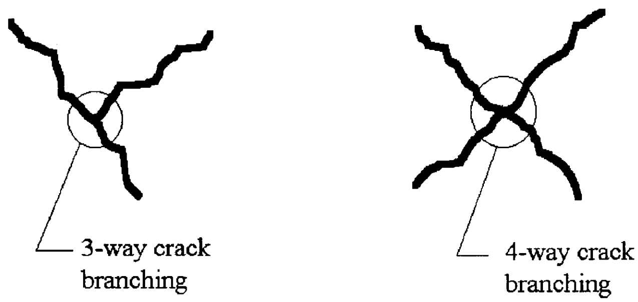

Fig. 20—3-way and 4-way crack-branching nodes.

specimens the average crack length was smaller in the center portion of the specimen than along the edge.

ACKNOWLEDGMENT

The authors would like to express their appreciation to Neville G. W. Cook and Larry R. Myer of the University of California at Berkeley for their guidance in designing the test apparatus and for advice on experimental procedures. Special thanks goes to William MacCracken of the Department of Civil Engineering for his insight and ingenuity in conducting the experiments, and to Stephen Laing and Adrian R. Brough of the Department of Material Science at the Imperial College in London for their help in computer programming and image processing. The study reported herein was funded through the grant MSM-8957183 from the National Science Foundation.

REFERENCES

1. Richart, F. E.; Brandtzaeg, A.; and Brown, L., "Study of the Failure of Concrete under Combined Compressive Stresses," *Bulletin* No. 185, University of Illinois Engineering Experiment Station, Urbana, 1929, p. 102.

2. Jones, R., "Method of Studying the Formation of Cracks in a Material Subject to Stresses," *British Journal of Applied Physics*, London, V. 3, No. 7, 1952, pp. 229-232.

3. L'Hermite, R., "Present Day Ideas in Concrete Technology, Part 3: The Failure of Concrete," *RILEM Bulletin*, 1954, pp. 27-38.

4. Hognestad, E.; Hanson, N. W.; and McHenry, D., "Concrete Stress Distribution in Ultimate Stress Design," Proceedings, *Journal of the American Concrete Institute*, 1955, pp. 455-479.

5. Czernin, W., *Chemistry and Physics of Cement for Civil Engineers*, Chemical Publishing Co., New York, 1962.

6. Hsu, T. T. C., "Mathematical Analysis of Shrinkage Stresses in a Model of Hardened Concrete," ACI JOURNAL, *Proceedings* V. 60, No. 3, 1963, pp. 371-390.

7. Hsu, T. T. C., and Slate, F. O., "Tensile Bond Strength between Aggregate and Cement Paste or Mortar," ACI JOURNAL, *Proceedings* V. 60, No. 4, 1963, pp. 465-486.

8. Hsu, T. T. C.; Slate, F. O.; Sturman, G. M.; and Winter, G., "Microcracking of Plain Concrete and the Shape of the Stress-Strain Curve," ACI JOURNAL, *Proceedings* V. 60, No. 2, 1963, pp. 209-224.

9. Slate, F. O., and Olsefski, S., "X-Rays for Study of Internal Structure and Microcracking of Concrete," ACI JOURNAL, *Proceedings* V. 60, No. 5, 1963, pp. 575-588.

10. Hamstad, M. A., "Review: Acoustic Emission, A Tool for Composite Materials Studies," *Experimental Mechechanics*, V. 26, No. 1, 1986, pp. 7-13.

11. Maji, A. K.; Ouyang, C.; and Shah, S. P., "Fracture Mechanics of Quasi-Brittle Materials Based on Acoustic Emission," *Journal of Materials Research*, V. 5, No. 1, 1990, pp. 206-217.

12. Ouyang, C.; Landis, E.; and Shah, S. P., "Damage Assessment in Concrete Using Quantitative Acoustic Emission," *ASCE Journal of Engineering Mechanics*, V. 117, No. 11, 1991, pp. 2681-2698.

13. Whitehurst, E. A., "Evaluation of Concrete Properties from Sonic Tests," *Monograph* No. 2, American Concrete Institute, Farmington Hills, Mich., 1966.

14. Monteiro, P. J. M., and King, M. S., "Experimental Studies of Elastic Wave Propagation in High-Strength Mortar," *ASTM Journal, Cement, Concrete, and Aggregates*, CCAGDP, V. 10, No. 2, 1988, pp. 68-74.

15. Orr, C. Jr., *Application of Mercury Penetration to Material Analysis, Powder Technology*, Elsevier Sequoia S.A., Lausanne, Switzerland, 1970, pp. 117-123.

16. Buyukozturk, O.; Nilson, A. H.; and Slate, F. O., "Stress-Strain Response and Fracture of Concrete Model in Biaxial Loading." ACI JOURNAL, *Proceedings* V. 68, 1971, pp. 590-599.

17. Buyukozturk, O.; Nilson, A. H.; and Slate, F. O., "Deformation and Fracture of a Particulate Composite," *Journal of Engineering Mechanics Division*, Proceedings of American Society of Civil Engineers, 1972, pp. 581-593.

18. Liu, T. C. Y.; Nilson, A. H.; and Slate, F. O., "Stress-Strain Response and Fracture of Concrete in Uniaxial and Biaxial Compression," ACI JOURNAL, *Proceedings* V. 69, 1972, pp. 291-295.

19. Carino, N. J., and Slate, F. O., "Limiting Tensile Strain Criterion for Failure of Concrete," ACI JOURNAL, *Proceedings* V. 73, 1976, pp. 160-65.

20. Martz, H. E.; Schneberk, D. J.; Roberson, G. P.; and Monteiro, P. J. M., "Computerized Tomography Analysis of Reinforced Concrete," *ACI Materials Journal*, V. 90, No. 3, May-June 1993, pp. 259-264.

21. Mobasher, B.; Castro-Montero, A.; and Shah, S. P., "Study of Fracture in Fiber-Reinforced Cement-Based Composites Using Laser Holographic Interferometry," *Experimental Mechanics*, V. 30, No. 3, 1990, pp. 201-207.

22. Maji, A. K., and Shah, S.P., "Measurement of Mixed-Mode Crack Profiles by Holographic Interferometry," *Experimental Mechanics*, V. 30, No. 2, 1990, pp. 201-207.

23. Regnault, P., and Bruhwiler, E., "Holographic Interferometry for the Determination of Fracture Process Zone in Concrete," *Engineering Fracture Mechanics*, V. 35, No. 1-3, 1990, pp. 29-38.

24. Yadev, G. D.; Dullien, F. A. L.; Chatzis, I.; and Macdonald, I. F., "Microscopic Distribution of Wetting and Non-Wetting Phases in Sandstone during Immiscible Displacements," *Paper* SPE 13212, presented at the 1984 SPE Annual Technical Conference and Exhibition, Dallas, Texas.

25. Pyrak, L. J., "Seismic Visibility of Fractures." PhD thesis, Depart-

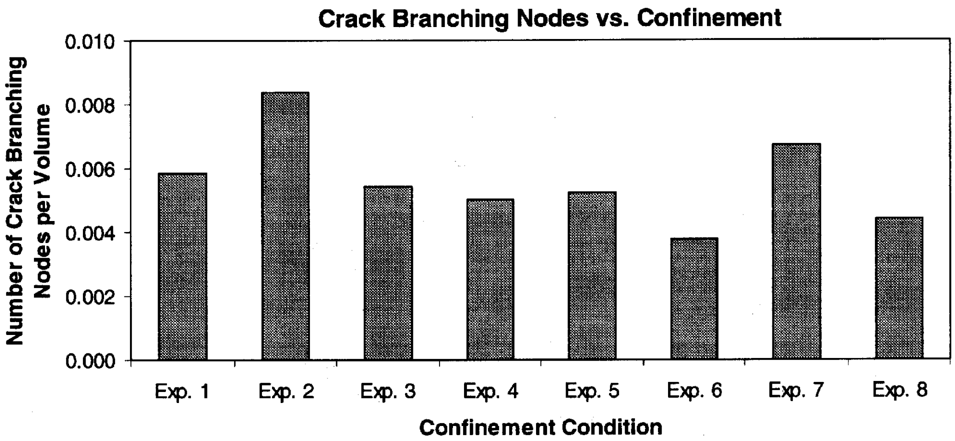

Fig. 21—Crack-branching nodes as a function of confinement for normal- and high-strength concrete

ment of Materials Science and Mineral Engineering, University of California at Berkeley, 1988.

26. Zheng, Z., "Compressive Stress-Induced Microcracks in Rocks and Applications to Seismic Anisotropy and Borehole Stability," PhD thesis, Department of Material Science and Mineral Engineering, University of California at Berkeley, 1989.

27. Stroeven, P., "Some Aspects of Micromechanics of Concrete," PhD thesis, Stevin Laboratory, Technological University of Delft, 1973.

28. Stroeven, P., "Application of Various Stereological Methods to the Study of the Grain and the Crack Structure of Concrete," *Journal of Microscopy*, V. 107, No. 3, 1976, pp. 313-321.

29. Stroeven, P., "Morphometry of Plain and Fibre Reinforced Concrete by Means of Image Analysis Techniques," *Proceedings of the Second International Conference on Mechanical Behavior of Materials*, Boston, Mass., 1976, pp. 1675-1679.

30. Stroeven, P., "Some Mechanical Effects of Interface Debonding in Plain Concrete, Interfaces in Cementitious Composites," *Proceedings of the RILEM International Conference*, Edited by J. C. Maso, Toulouse, France, 1992, pp. 187-196.

31. Ringot, E., "Automatic Quantification of Microcracks Network by Stereological Method of Total Projections in Mortars and Concretes," *Cement and Concrete Research*, V. 18, 1988, pp. 35-43.

32. Massat, M.; Ollivier, E.; and Ringot, E., "Microscopic Analysis of Microcracking Damage in Concrete and Durability," Laboratoire Materiaux et Durabilite des Constructions (INSA-UPS), Toulouse, France, 1988.

33. Nemati, K. M., "Generation and Interaction of Compressive Stress-Induced Microcracks in Concrete." PhD thesis, Department of Civil Engineering, University of California at Berkeley, 1994.

34. Nemati, K. M., and Monteiro, P. J. M., "Effect of Confinement on the Fracture Behavior of Concrete Under Compression," *Proceedings of the Second International Conference on Fracture Mechanics of Concrete and Concrete Structures*, FraMCoS, Zurich, Switzerland, V. 3, 1995, pp. 1843-1852.

35. Scrivener, K. L., and Nemati, K. M., "The Percolation of Pore Space in the Cement Paste/Aggregate Interfacial Zone of Concrete," *Cement and Concrete Research*, V. 26, No. 1, 1996, pp. 35-40.

36. Carpinteri, A.; Chiaia, B.; and Nemati, K. M., "Complex Fracture Energy Dissipation in Concrete under Different Loading Conditions," *Mechanics of Materials*, V. 26, No. 2, 1997, pp. 93-108.

37. Nemati, K. M., and Monteiro, P. J. M., "A New Method to Observe Three-Dimensional Fractures in Concrete Using Liquid Metal Prosimetry Technique," *Cement and Concrete Research*, V. 27, No. 9, 1997, pp. 1333-1341.

38. Nemati, K. M.; Monteiro, P. J. M.; and Cook, N. G. W., "New Method for Studying Stress-Induced Microcracks in Concrete Using Molten Metal Alloy," *Journal of Materials in Civil Engineering*, American Society of Civil Engineers, V. 10, No. 3, 1998, pp. 128-134.

39. Underwood, E. E., *Quantitative Stereology*, Addison-Wesley Publishing Co., New Jersey, 1968.

40. Gettu, R.; Bazant, Z. P.; and Karr, M. E., "Fracture Properties and Brittleness of High-Strength Concrete," *ACI Materials Journal*, V. 87, No. 6, Nov.-Dec. 1990, pp. 608-618.

41. Carrasquillo, R. L.; Nilson, A. H.; and Slate, F. O., "Properties of High-Strength Concrete Subject to Short-Term Loads," ACI JOURNAL, *Proceedings* 1981, pp. 171-178.

42. Kranz, R. L., "Microcracks in Rocks: A Review," *Tectonophysics*, V. 100, 1983, pp. 449-480.

43. Neville, A. M., *Properties of Concrete*, 4th Ed., John Wiley & Sons, Inc., New York, 1996.

44. Shah, S. P., and Chandra, S., "Fracture of Concrete Subjected to Cyclic and Sustained Loading," ACI JOURNAL, *Proceedings* V. 67, No. 10, pp. 816-825.

45. Shah, S. P., and Sankar, R., "Internal Cracking and Strain Softening Response of Concrete under Uniaxial Compression," *ACI Materials Journal*, V. 84, No. 3, Apr.-May 1987, p. 200.

46. Nakasa, K., and Nakatsuka, J., "Crack Initiation, Propagation and Branching in a Disk if Brittle Material under Axisymmetric Tension," *Engineering Fracture Mechanics*, V. 39, No. 4, 1991, pp. 661-670.

47. Nakasa, K. and Nakatsuka, J., "Analysis of Crack Branching Morphology in a Disk of Brittle Material under Axisymmetric Tension by Using Branching Dimension," *Engineering Fracture Mechanics*, V. 47, No. 3, 1994, pp. 403-415.

48. Mandelbrot, B. B., *Fractal Geometry of Nature*, W. H. Freeman, New York, 1977.